Bioconvective Vortices and Singular Bacterial Chemotaxis Near Contact Lines

Idan Tuval[1], Luis Cisneros[2], Christopher Dombrowski[2], Charles W. Wolgemuth[3] John O. Kessler[2], and Raymond E. Goldstein[2,4]

[1]Institut Mediterrani d'Estudis Avançats,
Consejo Superior de Investigaciones Cientificas,
Universitat de les Illes Balears, E-07071, Palma de Mallorca, Spain
[2]Department of Physics, University of Arizona, Tucson, AZ 85721
[3]Department of Cell Biology,
University of Connecticut Health Center, Farmington, CT 06030
[4]Program in Applied Mathematics, University of Arizona, Tucson, AZ 85721

Classifications:
Major – Physical Sciences
Minor – Applied Physical Sciences

Corresponding author:
Raymond E. Goldstein
Department of Physics
University of Arizona
1118 E. 4th St.
Tucson, AZ 85721
(520) 621-1065 (voice); (520) 621-4721 (fax)
gold@physics.arizona.edu

Manuscript information: 13 text pages; 6 figures; no tables
Total characters in paper=41,230
Number of words in abstract=128

Abstract

Aerobic bacteria often live in thin fluid layers near solid-air-water contact lines, where the biology of chemotaxis, metabolism, and cell-cell signaling is intimately connected to the physics of buoyancy, diffusion, and mixing. Using the geometry of a sessile drop we demonstrate in suspensions of *B. subtilis* the self-organized generation of a persistent hydrodynamic vortex which traps cells near the contact line. Arising from upward oxygentaxis and downward gravitational forcing, these dynamics are related to the Boycott effect in sedimentation, and are explained quantitatively by a mathematical model consisting of oxygen diffusion and consumption, chemotaxis, and viscous fluid dynamics. The vortex is shown to advectively enhance uptake of oxygen into the suspension and the wedge geometry leads to a singularity in the chemotactic dynamics near the contact line.

The interplay of chemotaxis and diffusion of nutrients or signaling chemicals in bacterial suspensions can produce a variety of structures with locally high concentrations of cells, including phyllotactic patterns (1), filaments (2), and concentrations in fabricated microstructures (3). Less well explored are situations in which concentrating hydrodynamic flows actually arise from these ingredients. Here we report a detailed experimental and theoretical study of an intriguing mechanism termed the *chemotactic Boycott effect*. Briefly described earlier (4), it is intimately associated with buoyancy-driven flows, metabolite diffusion, and slanted air-water meniscii. The ubiquity of contact lines and their transport singularities (5) suggest importance of these observations in biofilm formation (6). The large-scale stirring created by these flows illustrate important advective contributions to intercellular signaling, as in quorum sensing (7).

The chemotactic Boycott effect takes its name from a phenomenon in sedimentation (8) that occurs when the chamber containing a fluid with settling particles is tilted from vertical. Settling depletes the fluid near the upper wall, making it buoyant relative to nearby fluid, whereupon it rises. This boundary flow stirs up the entire medium, greatly accelerating the settling process. In the chemotactic version, negatively-buoyant aerobic bacteria swim up to the free surface of a sessile drop, and slide down the slanted meniscus, driving a hydrodynamic *vortex* in the region of the three-phase contact line that plays an important role in trapping cells. While counterintuitive in viscous flows, persistent circulation driven by forcing at the free surface is consistent with the classic analysis for vortex generation in wedge geometry (9).

Direct visualizations and particle-imaging-velocimetry (PIV) of the large-scale flows are presented here and compared quantitatively with results from a mathematical model that incorporates chemotaxis, oxygen transport and consumption, and viscous fluid dynamics. The characteristic fluid velocity U and length scale L associated with the vortex are both significantly larger than those of a single bacterium. In comparing the relative importance of advective to diffusive transport of a solute, it is natural to incorporate U, L, and the diffusion constant D into the dimensionless Peclet number $Pe = UL/D$. We find the Boycott-like flows lead to $Pe \gg 1$, indicating that advection dominates diffusion, just the opposite of the situation at the scale of a single bacterium. In addition, by analogy with evaporative singularities in sessile drops (5,10), we find a singularity in the oxygen uptake rate at the contact line. Along with the large-scale stirring of fluid in the drop, this significantly enhances the overall oxygen concentration in the medium, showing that collective effects can improve the viability of the population, as demonstrated by remarkable collective activity (4) of the extremely concentrated organisms near the drop edge.

Materials and Methods. Experiments were conducted with *B. subtilis* strain 1085B. Samples were prepared by adding 1 ml of -20° C stock to 50 ml of Terrific Broth (TB; Ezmix Terrific Broth, Sigma: 47.6g broth mix and 8 ml glycerin in 1 l dH_2O) and incubating for 18 h (shaker bath; 37° C, 100 rpm), after which 1 ml was added to 50 ml of TB and incubated for 5 h. The 5 h culture was then slowly added to the chamber with a syringe ($21G$ needle). The -20° stock was prepared by adding spores on sand to 10 ml. Terrific Broth at room temperature in a petri dish and allowing for $\sim$ 24 h of growth. 1 ml of 24 h stock was added to 50 ml TB and incubated for 18 h. 1 ml of the 18 h culture was added to 50 ml of TB and incubated 5 h. Aliquots composed of 0.75 ml of 5 h culture mixed gently with 0.25 ml glycerin were placed in cold storage. The chambers (Fig. 1A) were constructed from microscope slides cemented together with UV-curing adhesive (Norland); care was taken to remove excess adhesive to avoid interference with visualizations near the contact line, and to seal the chamber adequately to avoid evaporation and associated flows. Imaging was achieved with a digital ccd camera (Hamamatsu C7300, 1024×1024 pixels, 12 bit) under computer control (National Instruments), attached to a macrophotography bellows (PB-6, Nikon) with a 105 mm f/2.8 lens. Darkfield illumination was a 4 cm diameter fiber optic ring light (Navitar) behind the sample chamber. PIV measurements were conducted by adding 5 μl of fluorescent microspheres (Molecular Probes, F8825 Carboxylate-modified, 1.0 μm, Nile red) to 1 ml of suspension, illuminating with a DPSS laser (100 mW, 532 nm) reflected from a dichroic mirror (Z542RDC, Chroma Technology), and visualizing through a long-pass filter (HQ542LP, Chroma). Analysis was performed with PIV software (Dantec Dynamics).

Results. Figures 2A-C show images of the main stages of the chemotactic Boycott effect. After a drop of well-mixed suspension is placed in the chamber, the first spatial structure that forms is a "depletion layer" of thickness $\ell \sim 1$ mm below the fluid-air interface, which appears dark in our imaging method because of the absence of cells. This region arises from the consumption of dissolved oxygen by the uniformly dispersed cells, followed by their chemotactic migration up the oxygen gradient to the source of oxygen - the free surface. No cellular motion is seen below the depletion layer, suggesting that the oxygen concentration there has fallen to the critical value, denoted c^*, below which motility vanishes. In a flattened sessile drop the bottom of the depletion layer follows the shape of the air-water meniscus, displaced downward by the layer thickness. This layer forms within 100 s, consistent with consumption of the saturation dissolved oxygen concentration $c_s \sim 10^{17}$ cm^{-3} by cells at concentration $n_0 \sim 10^9$ cm^{-3}, with a consumption rate $\kappa \sim 10^6$ oxygen molecules per second. This is also consistent with the time $t_\ell = \ell/v_c$ for a cell with a typical chemotactic velocity

$v_c \sim 10\mu$m/s to traverse the thickness ℓ. Ultimately, the cells congregate in a narrow surface "accumulation layer" whose thickness $d \sim 100\mu$m.

While the accumulation layer slides along the meniscus to the contact line it is unstable to plume formation on a length scale comparable to the layer thickness, consistent with the fundamental instability of bioconvection in fluids with a horizontal meniscus (11). The Boycott effect occurs at the slant region; the resultant surface and return flows distort the plumes that would otherwise fall straight down. This surface flow is opposite to that of the conventional Boycott effect, whereas the depletion layer here is buoyantly forced in the usual direction, creating a unique shear double layer. Typical fluid velocities at the free surface are in the range $20 - 200$ μm/s, accelerating as the meniscus slope increases near the contact line. Finally, due to incompressibility requirements, a well-developed vortex appears near each of the contact lines and shows persistence over many tens of minutes. The closed streamlines (Fig. 3A) show the sense of circulation created by the downward gravitational forcing on the accumulation layer and the recirculation into the bulk required by fluid incompressibility. Despite the outward flow at the bottom of the vortex, the optical density indicates that cells are trapped near the contact line.

Mathematical Model. The dynamics of the oxygen concentration c, cell concentration n, and fluid velocity $\mathbf{u}$, are described by coupled PDEs (12),

$$c_t + \mathbf{u}\cdot\boldsymbol{\nabla} c = D_c\nabla^2 c - n\kappa f(c) \quad (1)$$

$$n_t + \mathbf{u}\cdot\boldsymbol{\nabla} n = D_n\nabla^2 n - \boldsymbol{\nabla}\cdot[\mu r(c)\, n\boldsymbol{\nabla} c] \quad (2)$$

$$\rho(\mathbf{u}_t + \mathbf{u}\cdot\boldsymbol{\nabla}\mathbf{u}) = -\boldsymbol{\nabla} p + \eta\nabla^2\mathbf{u} - \mathrm{V_b} g n \Delta\rho\hat{\mathbf{z}}\ . \quad (3)$$

In (1) the oxygen diffusion constant is $D_c \sim 2\times 10^{-5}$ cm^2/s, and the dimensionless function $f(c)$ modulates the oxygen consumption rate κ, asymptoting to unity at large c, but vanishing as $c \to 0$. As the experimental timescales are minutes and the cell division time is ~ 100 minutes, the dynamics (2) of n conserve the total number of cells. The bacterial diffusion constant D_n arises as a consequence of the random swimming trajectories and is estimated to be $D_n \sim 10^{-6} - 10^{-5}$ cm^2/s. Chemotaxis is described by the second term on the r.h.s. of (2), with a velocity proportional to the oxygen gradient (13); the coefficient μ may be interpreted as $\mu = av_0/c_s$, so that the chemotactic velocity is v_0 when the gradient is c_s/a, where a is a characteristic length. Like the function $f(c)$, the motility function $r(c)$ is unity at large c and vanishes rapidly for c below the motility cutoff c^*; we approximate it and $f(c)$ by the step function $\Theta(c-c^*)$. Subject to incompressibility, $\boldsymbol{\nabla}\cdot\mathbf{u} = 0$, the fluid equations (3) utilize the Boussinesq approximation in which the density variations due to bacteria appear only in the buoyant forcing, with $\Delta\rho = \rho_b - \rho$, where $\mathrm{V_b}$ and ρ_b are the

bacterial volume and density and ρ is the pure fluid density.

The boundary conditions on c, n, and $\mathbf{u}$ are central to the global flows and possible singularities. As shown in Fig. 1B, there is no flux (of cells or of oxygen) through the substrate, under the drop and to its side, and no cell flux through the fluid-air interface. That interface is stress-free, while the fluid-glass boundary has no slip. Since the oxygen diffusion coefficient in the air is three orders of magnitude larger than that in the fluid, the oxygen concentration outside the drop can be assumed equal to its saturation value c_s inside the fluid and on the free surface. Oxygen diffusion in the drop is equivalent to that in the enlarged space whose bottom is the reflection of the meniscus across the fluid-glass interface. This lens-shaped region has a sharp point which is the source of a chemotactic singularity in the same way that a pointed electrical conductor produces a singular electric field.

We rescale (1)-(3) to identify the dimensionless control parameters. If $L \sim 0.1$ cm is the depth of the drop, we define the rescaled variables $\mathbf{x} = \mathbf{r}/L$, $s = D_n t/L^2$, $\chi = c/c_s$, $\rho = n/n_0$, $\pi = L^2 p/\eta D_n$, $\mathbf{v} = L\mathbf{u}/D_n$. Defining $\delta = D_c/D_n \sim 1 - 10$, and $\alpha = a v_0/D_n \sim 10$, we have

$$\chi_s + \mathbf{v}\cdot\boldsymbol{\nabla}\chi = \delta\nabla^2\chi - \rho\beta f(\chi) \tag{4}$$

$$\rho_s + \mathbf{v}\cdot\boldsymbol{\nabla}\rho = \nabla^2\rho - \alpha\boldsymbol{\nabla}\cdot[r(\chi)\,\rho\boldsymbol{\nabla}\chi] \tag{5}$$

$$\frac{1}{Sc}(\mathbf{v}_s + \mathbf{v}\cdot\boldsymbol{\nabla}\mathbf{v}) = -\boldsymbol{\nabla}\pi + \nabla^2\mathbf{v} - \gamma\rho\hat{\mathbf{z}} \tag{6}$$

where

$$\beta = \frac{\kappa n_0 L^2}{c_s D_n} \qquad Sc = \frac{\nu}{D_c} \quad \gamma = \frac{v n_0 g(\rho_b - \rho)L^3}{\eta D_n}\ . \tag{7}$$

The time $L^2/D_n \sim 10^3$ s is that for diffusion across the drop, $\beta \sim 10$ is the ratio of the bacterial diffusion time to that for oxygen consumption, and the Schmidt number $Sc \sim 10^3$ measures the importance of viscosity to diffusion of oxygen. Finally, $\gamma \sim 10^3$ is analogous to the Rayleigh number in thermal convection (11).

Comparison With Experiment. The phenomena shown in Figs. 2 and 3 can now be explained, beginning with formation of the depletion and accumulation layers. Forming first in the absence of fluid flow, we need only consider Eqs. 1 and 2 with $\mathbf{u} = 0$, and even more simply in a one-dimensional vertical cut through the drop. Quasi-steady-state profiles of c and n are found in which c varies exponentially down from the free surface until it intercepts c^*. From this one deduces

$$\ell = \left(\frac{D_c\,(1-c^*)\,c_s}{\kappa n_0}\right)^{1/2}\ , \qquad d = \frac{D_n}{v_c}\ . \tag{8}$$

The result $\ell \sim n_0^{-1/2}$ can be verified by a dilution experiment. Figs. 4B & C show two drops, the first from the standard bacterial suspension with cell concentration n_0, the second a dilution to $0.4n_0$. The increase in ℓ is apparent. Vertical traces of the optical intensity through the height of the drop, averaged over 40 s, yield profiles like that shown in Fig. 4D, from which ℓ is determined. We see good agreement with the numerical results in Fig. 4A although at the very high cell concentrations in the accumulation layer the optical intensity saturates, the likely explanation for the relatively small intensity there. With parameters discussed above, we fit ℓ for the undiluted solution with $c^* = 0.3c_s$, and then ℓ of the diluted solution lies accurately on the prediction (Fig. 4E).

Numerical studies of the PDEs with a curved fluid-air interface are readily accomplished with finite-element methods. Calculations were done with Femlab (Comsol, Inc.). The coupled PDEs for handled using the "general" form, with high order Lagrange elements (quintic for Eqs. 4 & 5 and quartic-quadratic for Eq. 6), on a triangular mesh consisting of ~ 1000 nodes, and a fifth-order time integration scheme in the nonlinear time-dependent solver. We focus here on two-dimensional dynamics, equivalent to the assumption of translational invariance with respect to the direction *along* the contact line. The essential features of the flow are found as well in numerical studies using Darcy's law for flow between the vertical plates of the experimental chamber. Overhead views of sessile drops reveal that in the third dimension the vortex breaks up into a radial form of bioconvective plumes (4). Elsewhere we discuss these in more detail. Our two-dimensional computations, shown in Figs. 2A'-C', reproduce the observations; the depletion layer tracing the shape of the meniscus, the variations in thickness of the accumulation layer over the boundary of the drop, and the plume instability. Figure 3B shows that the vortex is also captured accurately.

Except close to the contact line, the accumulation layer is very thin compared to the depth of the drop, so the gravitational forcing that acts on it is essentially concentrated at the surface. When combined with the no-slip boundary condition at the bottom of the drop, this defines one of the scenarios in Moffatt's analysis of viscous eddies in sharp corners (9). Theory predicts a set of progressively smaller vortices adjacent to the main vortex. We have not seen evidence of these, either in experiment or simulations, but they are expected to be extremely weak and are likely outside the resolution of both approaches. Theory also suggests that the conditions under which vortices develop can depend sensitively on the far-field conditions and the wedge angle. Our numerical results indicate the existence of a vortex at least over a range of angles from $\pi/4$ to $\pi/2$.

The velocities U in the vortex can reach 0.01 cm/s, with a size of 0.1 cm, so the

Peclet number can approach $\sim 10^2$. Numerical studies show that the combination of accumulated bacteria and greatly-enhanced stirring in the wedge lead to (i) a near-singular variation in oxygen flux near the contact line (Fig. 5A), and (ii) an increase in oxygen uptake into the drop. Figure 5B shows that the average oxygen concentration initially drops precipitously as consumption dominates, but it slowly returns to a high value as stirring enhances the uptake from the air above. Without the hydrodynamic coupling between cell concentration and buoyancy, the oxygen concentration remains low after the initial consumptive drop. Not only oxygen, but also nutrients will be ferried to the contact line region from areas in the bulk of the drop.

Chemotactic Singularity. Some insight into the oxygen flux near the contact line is obtained by making use of the electrostatic analogy mentioned above. The simplest steady-state oxygen diffusion problem, for which $\nabla^2 c = 0$ inside the drop and $c = c_s$ on the free surface, is mathematically equivalent to the equation defining the electrostatic potential in that same region, the exterior of the drop being a conductor (5). This mapping reveals (14) that a singularity arises from a solution of the form

$$c(r,\phi) \sim c_s + \sum_{m=1}^{\infty} a_m r^{m\pi/2\theta} \cos(m\pi\phi/2\theta) \ , \tag{9}$$

with polar coordinates (r,ϕ) as in Fig. 1B. This form enforces the condition $c = c_s$ on the drop surface ($\phi = \theta$) and the no-flux condition on the glass substrate ($\phi = 0$). Upon successive differentiation, the potentially most singular term is $m = 1$, and we expect $a_1 < 0$ since $c \leq c_s$ in the drop interior. Noting that $|\boldsymbol{\nabla} c| \sim r^{\pi/2\theta - 1}$ and $\nabla^2 c \sim r^{\pi/2\theta - 2}$, singularities appear in two cases:

1. $\theta > \pi/2$, an overhanging meniscus. This case is like the familiar "lightning rod" effect. Both the Fick's law oxygen flux, $-D_c \boldsymbol{\nabla} c$, and the chemotactic flux, $\mu r n \boldsymbol{\nabla} c$, diverge as $r \to 0$, leading to a singular accumulation at the contact line.

2. $\pi/4 < \theta < \pi/2$, as in Figs. 2-4: Here, $\nabla^2 c$ diverges as $r \to 0$. Expanding the chemotaxis term in the dynamics (3), we see terms of the form $\mu r[\boldsymbol{\nabla} n \cdot \boldsymbol{\nabla} c + n \nabla^2 c]$, the latter implying that the time derivative of the cell density n diverges. Although weaker than case 1, there still is a singular accumulation driven by the diffusional singularity of oxygen.

Let us consider in more detail the typical case $\theta < \pi/2$. There is a positive, bidirectional feedback loop involving the chemotactic response to the oxygen singularity.

The singularity is reinforced by the accumulation of bacteria which consume the oxygen. A rough idea of this can be gleaned by examining a steady state balance between the dominant terms in the chemotaxis equation (2), setting $D\nabla^2 n \sim \mu r n \nabla^2 c$ to find a distribution $n \sim \exp(-\Gamma r^{\pi/2\theta})$, with $\Gamma > 0$, that decays away from the contact line very sharply. Since the local oxygen consumption rate is proportional to n, the inward flux of oxygen mirrors the bacterial concentration distribution, as in Fig. 5B. While a more precise treatment requires a fully self-consistent calculation of the coupled oxygen and bacterial concentrations, this result illustrates the dramatic accumulation of bacteria in the contact region.

The development of the self-trapping vortex and the associated high concentration of bacteria near the contact line depend crucially on the no-flux boundary conditions at the substrate. A dramatic demonstration of this is seen in the flows in a "supported" drop. This geometry was achieved by turning over the experimental chamber, allowing a previously sessile drop to slide down from the chamber base toward the opening at the opposite end. Surface tension supports the drop, with free uptake of oxygen around the whole meniscus. As shown in Fig. 6, the bottom interface is very flat, giving an effective contact angle exceeding $\pi/2$, but with no substrate the dynamics are nonsingular. We see the key stages in the chemotaxis and fluid instabilities in this geometry. Development of the depletion zone occurs rather symmetrically around the entire perimeter of the drop, producing the non-motile region in the center. Later, plumes descend from above and the accumulation layer slides down the drop meniscus, producing a clearly visible enhancement of concentration at the bottom of the meniscus beyond the local chemotactic concentration. The computations quantitatively reproduce these features.

At the high concentrations found near the contact line of sessile drops or at the bottom of supported drops the viscous drag between the fluid and bacteria is comparable to that of the fluid on itself. A simple estimate gives the volume fraction φ^* at which this transition takes place. The drag force per unit volume on the suspension is $\zeta u^b \varphi / \mathrm{V_b}$, with $\zeta = 6\pi\eta R$ the drag coefficient of an equivalent sphere of radius R, u^b the bacterial velocity, and $V_b = 4\pi R^3/3$ the equivalent volume of a bacterium. The viscous drag force on the fluid per unit volume is $\eta u^f / L^2$, where L is a characteristic scale of the flow and u^f the fluid velocity. Equating these two gives

$$\varphi^* = \frac{2}{9}\left(\frac{R}{L}\right)^2 \frac{u^f}{u^b} \ , \tag{10}$$

independent of viscosity. Taking $R \sim 2$ μm as a representative bacterium radius and $L \sim 100$ μm, the thickness of the accumulation layer, and $u^f/u^b \sim 5$ (4), then $\varphi* \sim 5 \times 10^{-4}$, corresponding to a concentration $n \sim 5 \times 10^8$ cm^{-3}, comparable

to a typical initial homogeneous concentration in the drop. For volume fractions in excess of φ^*, the fluid and bacterial velocities should be treated equally; one method to accomplish this uses two-phase fluid flow (15). With the low Reynolds numbers of the typical flows, the coupled dynamics of the bacterial and fluid velocities $\mathbf{u}^b$ and $\mathbf{u}^f$ are

$$\zeta\left(\mathbf{u}^f - \mathbf{u}^b\right) = -(1-\varphi)\boldsymbol{\nabla} p + \eta^f \nabla^2 \mathbf{u}^f \tag{11}$$

$$\zeta\left(\mathbf{u}^b - \mathbf{u}^f\right) = -\varphi\boldsymbol{\nabla} p - \frac{D_b}{\varphi}\boldsymbol{\nabla}\varphi - \Delta\rho g\hat{\mathbf{z}} + \mu r \boldsymbol{\nabla} c \tag{12}$$

with the continuity condition, $\boldsymbol{\nabla}\cdot\left(\varphi\mathbf{u}^b + (1-\varphi)\mathbf{u}^f\right) = 0$. Numerical investigations of (11) and (12) coupled to the oxygen dynamics (1) show qualitatively similar results for the overall bioconvective flows to those obtained with the Navier-Stokes equations (3), but as well provide a more quantitatively correct description of the dense regime.

Conclusions. We have shown that the interplay of chemotaxis, buoyancy, and meniscus geometry is responsible for persistent fluid circulation and high cell densities in the neighborhood of contact lines. This circulation is strong enough to render advection dominant over diffusion and enhance the overall oxygen uptake into the medium. Driven entirely by chemotaxis and metabolism of individual cells, no explicit cell-cell communication is necessary for these phenomena to occur. Nevertheless, the creation of a micro-ecological structure by a self-organized dynamic will likely influence concurrent cell-cell communication which is necessary for such processes as quorum sensing and subsequent biofilm formation (16).

We are grateful to K. Glasner for important discussions. This work was supported in part by NSF MCB0210854 (LC,CD,JOK,REG), NSF MCB 0327716 and NIH R01 GM072004 (CW), and the Spanish Ministerio de Ciencia y Tecnologia, contract BFM2000-1108 (CONOCE) (IT).

References

[1] Budrene, E. O. & Berg, H. C. (1995) *Nature* **376**, 49-53.

[2] Betterton, M. D. & Brenner, M. P. (2001) *Phys. Rev. E* **64**, 061904-1-15.

[3] Park, S., Wolanin, P. M., Yuzbashyan, E. A., Silberzan, P., Stock, J. B. & Austin, R. H. (2003) *Science* **301**, 188.

[4] Dombrowski, C., Cisneros, L., Chatkaew, S., Kessler, J. O. & Goldstein, R.E. (2004) *Phys. Rev. Lett.* **93**, 098103-1-4.

[5] Deegan, R. D., Bakajin, O., Dupont, T. F., Huber, G., Nagel, S. R. & Witten, T. A. (1997) *Nature* **389**, 827-829.

[6] O'Toole, G., Kaplan, H. B. & Kolter, R. (2000) *Annu. Rev. Microbiol.* **54**, 49-79.

[7] Bassler, B. L. (2002) *Cell* **109**, 421-424.

[8] Boycott, A. E. (1920) *Nature* **104**, 532.

[9] Moffatt, H. K. (1964) *J. Fluid Mech.* **18**, 1-18.

[10] Deegan, R. D., Bakajin, O., Dupont, T. F., Huber, G., Nagel, S. R. & Witten, T. A. (2000) *Phys. Rev. E* **62**, 756-765.

[11] Pedley, T. J. & Kessler, J. O. (1992) *Annu. Rev. Fluid Mech.* **24**, 313-358.

[12] Hillesdon, A. J., Pedley, T. J. & Kessler, J. O. (1995) *B. Math. Biol.* **57**, 299-344.

[13] Keller, E. F. & Segel, L. A. (1971) *J. Theor. Biol.* **30**, 225-234.

[14] Jackson, J. D. (1962) *Classical Electrodynamics* (Wiley, New York).

[15] Drew, D. A. & Segel, L. A. (1971) *Stud. Appl. Math.* **50**, 205-231.

[16] Davies, D. G., Parsek, M. R., Pearson, J. P., Iglewski, B. H., Costerton, J. W. & Greenberg, E. P. (1998) *Science* **280**, 295-298.

Figure Captions

Figure 1. (A) Apparatus for simultaneous darkfield and fluorescence imaging of fluid drops. Laser (L), shutter (S), beam expander lenses (L_1 & L_2), dichroic beam-splitter (D), long-pass filter (LPF), fiber-optic ring light (RL), digital camera (C). Chamber has anti-reflection areas (AR) to reduce glare and hydrophobic areas (H) to pin the drop. (B) Boundary conditions and coordinates in the wedge, described in text.

Figure 2. Stages leading to self-concentration in a sessile drop, observed experimentally (left) and by numerical computations with the model described in text (right). (A,A') drop momentarily after placement in chamber. (B,B') formation of depletion zone after 150 s, prior to appreciable fluid motion, (C,C') lateral migration of accumulation layer toward drop edges and creation of vortex (shown in Fig. 3), after 600 s. Color scheme describes the rescaled bacteria concentration ρ. Scale bar is 0.5 mm.

Figure 3. Hydrodynamic vortex near three-phase contact line. (A) velocity contours obtained from PIV measurements, averaged over 750 frames acquired at intervals of 0.2 s. Scale bar is 1 mm. Region immediately above PIV contours is the curved fluid-air interface beyond the slice viewed in cross section. (B) Numerical results obtained from finite-element calculations using the model in Eqs. 1-3. Closed streamlines are shown along with velocity magnitude in color.

Figure 4. Depletion layers in sessile drops. (A) Numerical solution of (1) and (2) for the rescaled cell concentration as a function of rescaled height. (B) depletion layer forming in stock solution and (C) in a 40% dilution. Scale bar is 0.5 mm. (D) averaged intensity trace in the stock solution, normalized to intensity at bottom of drop. (E) depletion layer thickness as a function of relative concentration. Dashed line is theoretical prediction.

Figure 5. Oxygen dynamics from numerical studies. (A) Inward flux of oxygen along upper surface of a drop, in units of $D_c c_s/L$, as a function of distance r from the contact line, showing near-singular behavior. (B) Average oxygen concentration in the drop as a function of rescaled time s, normalized to initial value.

Figure 6. Self-concentration in a thin droplet, confined between glass plates, surrounded by air. Experimental observations and numerical results presented as in Fig. 2, with (A,A') at time $t = 0$, (B,B') at 200 s, and (C,C')=360 s. Scale bar is 0.5 mm

Figures

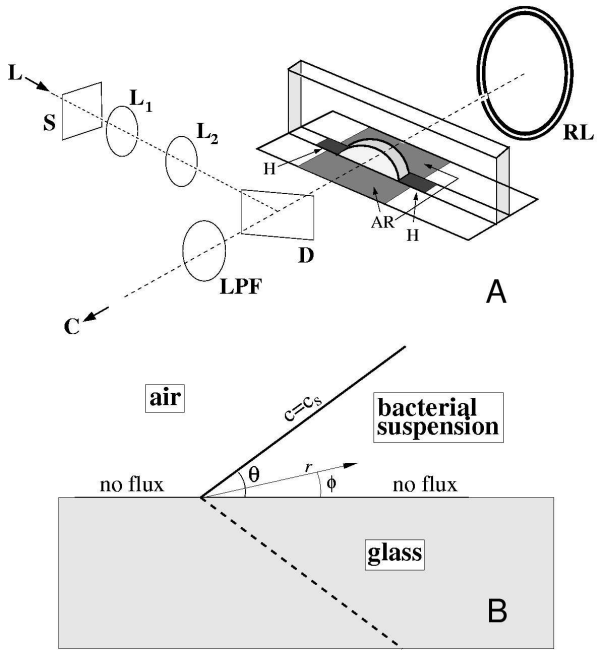

Figure 1. (A) Apparatus for simultaneous darkfield and fluorescence imaging of fluid drops. Laser (L), shutter (S), beam expander lenses (L_1 & L_2), dichroic beam-splitter (D), long-pass filter (LPF), fiber-optic ring light (RL), digital camera (C). Chamber has anti-reflection areas (AR) to reduce glare and hydrophobic areas (H) to pin the drop. (B) Boundary conditions and coordinates in the wedge, described in text.

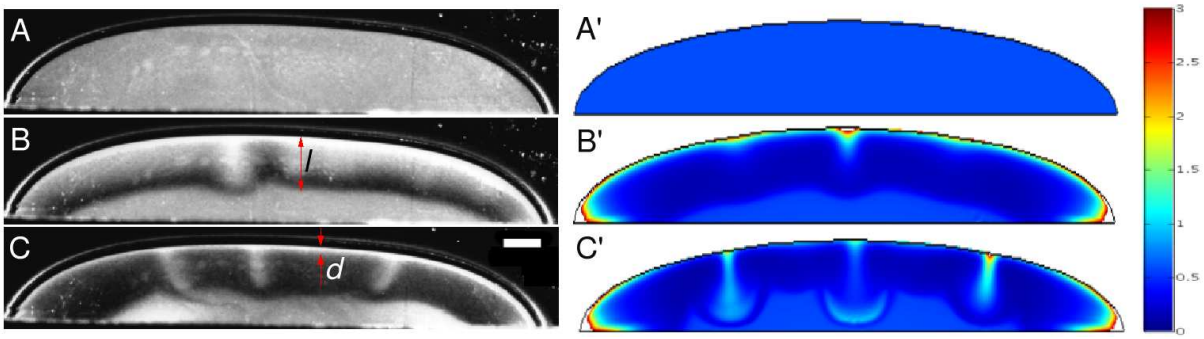

Figure 2. Stages leading to self-concentration in a sessile drop, observed experimentally (left) and by numerical computations with the model described in text (right). (A,A') drop momentarily after placement in chamber. (B,B') formation of depletion zone after 150 s, prior to appreciable fluid motion, (C,C') lateral migration of accumulation layer toward drop edges and creation of vortex (shown in Fig. 3), after 600 s. Color scheme describes the rescaled bacteria concentration ρ. Scale bar is 0.5 mm.

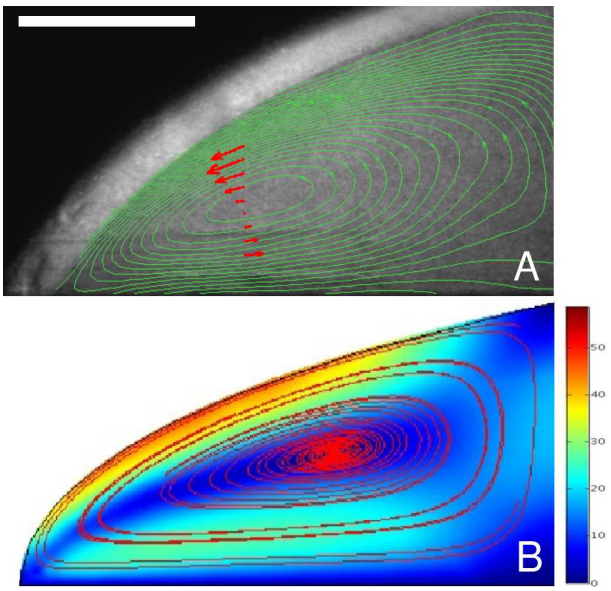

Figure 3. Hydrodynamic vortex near three-phase contact line. (A) velocity contours obtained from PIV measurements, averaged over 750 frames acquired at intervals of 0.2 s. Scale bar is 1 mm. Region immediately above PIV contours is the curved fluid-air interface beyond the slice viewed in cross section. (B) Numerical results obtained from finite-element calculations using the model in Eqs. 1-3. Closed streamlines are shown along with velocity magnitude in color.

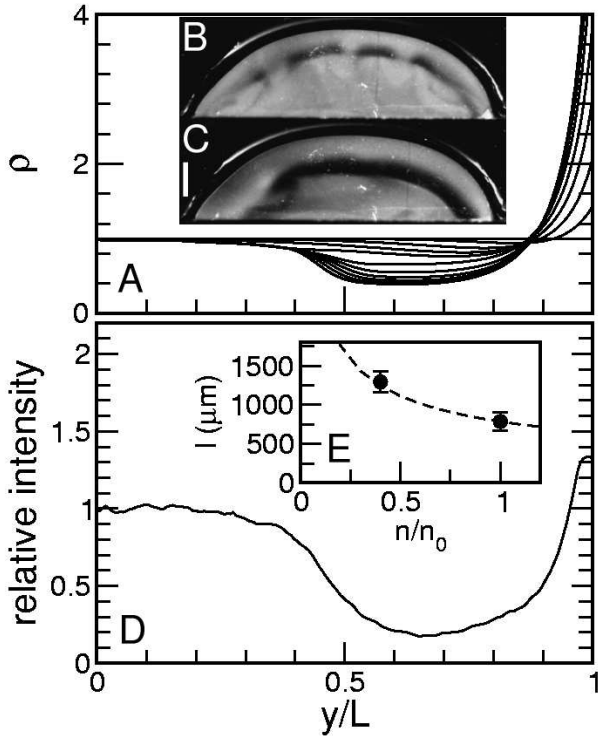

Figure 4. Depletion layers in sessile drops. (A) Numerical solution of (1) and (2) for the rescaled cell concentration as a function of rescaled height. (B) depletion layer forming in stock solution and (C) in a 40% dilution. Scale bar is 0.5 mm. (D) averaged intensity trace in the stock solution, normalized to intensity at bottom of drop. (E) depletion layer thickness as a function of relative concentration. Dashed line is theoretical prediction.

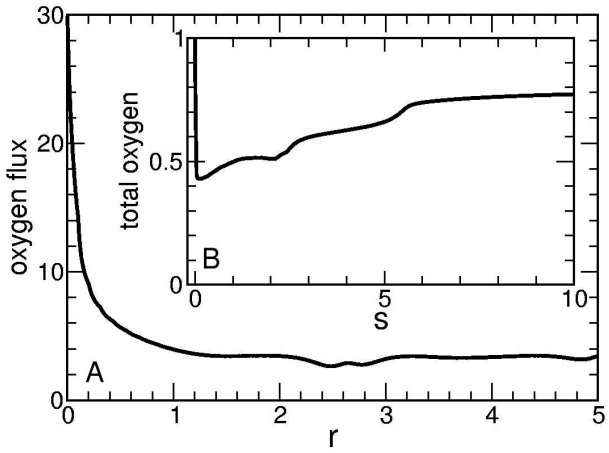

Figure 5. Oxygen dynamics from numerical studies. (A) Inward flux of oxygen along upper surface of a drop, in units of $D_c c_s/L$, as a function of distance r from the contact line, showing near-singular behavior. (B) Average oxygen concentration in the drop as a function of rescaled time s, normalized to initial value.

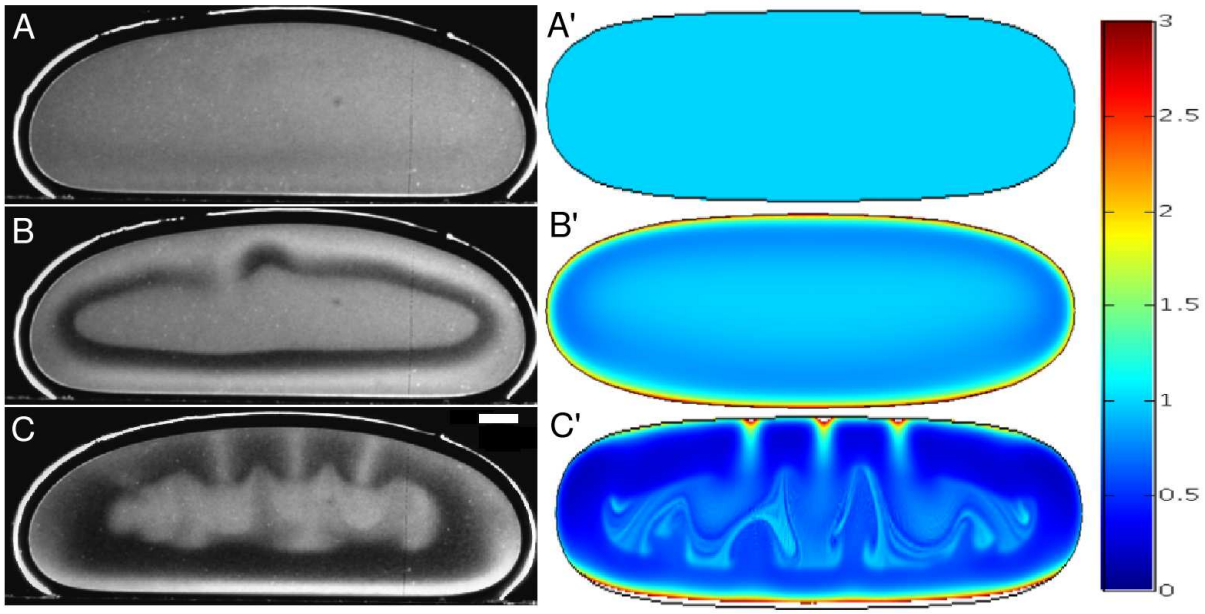

Figure 6. Self-concentration in a thin droplet, confined between glass plates, surrounded by air. Experimental observations and numerical results presented as in Fig. 2, with (A,A') at time $t = 0$, (B,B') at 200 s, and (C,C')=360 s. Scale bar is 0.5 mm